ISSN 1029-9599, Physical Mesomechanics, 2015, Vol. 18, No. 3, pp. 261–272. © Pleiades Publishing, Ltd., 2015.
Original Russian Text © S.V. Panin, I.V. Vlasov, V.P. Sergeev, B.B. Ovechkin, P.O. Marushchak, Sunder Ramasubbu, P.S. Lyubutin, V.V. Titkov, 2014, published in Fizicheskaya Mezomekhanika, 2014, Vol. 17, No. 4, pp. 97–110.

Fatigue Life Enhancement by Irradiation of 12Cr1MoV Steel with a Zr^+ Ion Beam. Mesoscale Deformation and Fracture

S. V. Panin[1,2]*, I. V. Vlasov[1,2], V. P. Sergeev[1,2], B. B. Ovechkin[2], P. O. Marushchak[3], Sunder Ramasubbu[2,4], P. S. Lyubutin[1], and V. V. Titkov[1]

[1] *Institute of Strength Physics and Materials Science, Siberian Branch, Russian Academy of Sciences, Tomsk, 634055 Russia*
[2] *National Research Tomsk Polytechnic University, Tomsk, 634050 Russia*
[3] *Ternopol National Technical University, Ternopol, 46001 Ukraine*
[4] *Bangalore Integrated System Solutions Pvt. Ltd., Peenya Industrial Area, Bangalore, 560058 India*
* *e-mail: svp@ispms.tsc.ru*

Received March 21, 2014

Abstract—The structure and properties of 12Cr1MoV steel irradiated with a zirconium ion beam were studied by optical microscopy, scanning electron microscopy, and micro- and nanoindentation. It is shown that the modification covers the entire cross-section of the irradiated specimens to a depth of 1 mm. The data on irradiation-induced structural changes are used to interpret the changes in mechanical properties of the irradiated specimens under static and cyclic loading. Particular attention is given to analysis of strain estimation by the digital image correlation method.

DOI: 10.1134/S1029959915030108

Keywords: fatigue life, ion beam treatment, surface nanostructuring, deformation, fracture, digital image correlation

1. INTRODUCTION

In one of our previous papers we studied the influence of irradiation of heat-resistant 12Cr1MoV steel with a Zr^+ ion beam on its mechanical properties and fatigue life [1]. Most attention was focused on assessment of structural modification in a thin layer of a few micrometers. Transmission electron microscopy and X-ray diffraction analysis revealed the presence of intermetallic and carbide compounds, substantial grain refinement in the thin specimen layer after irradiation, and formation of phases with a size of 100–150 μm. Particular attention was given to analysis of the processes occurring on the surface because it was evident that the untreated and treated specimens differed in their deformation relief. It was found that fracture of the modified layer involved cracking only in a small area which experienced substantial thinning (necking). At the same time, the deformation relief in the modified layer was much less pronounced compared to the untreated specimens, as was evidenced by measurement data on the roughness at different distances from the necking site.

Tests for static and cyclic tension revealed an increase in ultimate strength by 15% and in fatigue life by a factor of 2 or 3. It was supposed that a possible cause for the observed effects was multiple microcracking capable of providing substantial dispersion of powerful stress concentrators and impediment of strain macrolocalization. However, multiple cracking was observed only in individual regions. Moreover, the steel matrix (core) displayed considerable ductility which could compensate to a certain degree the negative influence of cracks as stress concentrators (notches).

Thus, the data obtained in our previous study and their explanations [1] are insufficient for understanding the multiscale nature of the observed phenomena. Therefore, our further research was focused on studying the structural changes not only in thin surface layers but also beneath them, including core regions. A more detailed

analysis was performed to study the mechanisms of deformation under static and cyclic loading.

The strain-induced behavior of 12Cr1MoV steel before and after ion beam treatment was studied using a TOMSC television-optical measuring complex based on an Instron-5288 electromechanical testing machine. For estimation of meso- and macroscale strains, we used the digital image correlation (DIC) method [2], allowing one to obtain qualitative and quantitative strain distribution patterns (displacement vector fields, shear strain intensity, and its integral value over a surface under study).

2. MATERIAL AND RESEARCH TECHNIQUE

The test material was chosen due to its heat resistance for minimizing the thermal effect of ion beam treatment. The proposed method of modification can be recommended for continuous casting rolls made of 25Cr1Mo1V steel [3, 4], which is similar in purpose and properties to 12Cr1MoV and is intended for operation at high temperatures (570–585°C) [5]. The test material was spark cut from a steam pipeline to obtain flat specimens of dimensions $70\times10\times1$ mm^3. For fatigue tests, a hole of diameter 2 mm was drilled in the specimens at 50 mm from one of the edges. The specimens for static tension were dumbbell shaped to have a double gage section of dimensions $20\times5\times1$ mm^3 (first section) and $3\times5\times1$ mm^3 (second section). The specimen shape allows direct observation of strain localization in tension and quantitative estimation of mesoscale strains on the specimen surface by the DIC method.

Like in our previous study [1], the test specimens were in the as-received state (untreated) and subjected to irradiation with a Zr^+ ion beam (treated) on a UVN-02 Kvant high-current vacuum arc source of metal ions [6]. When treated, the surface layer of the specimens experienced short-time heating to temperatures of about 600–900°C. However, due to rotation of the specimens with respect to the ion source (Fig. 1), their surface heating (which occurred at instant of interaction with the ion beam) was not continuous and this eliminated heat-induced softening (tempering). The specimens experienced a certain degree of cyclic thermal action which was bound to result in structural changes not only in their modified thin surface layer but also beneath it.

The specimen microstructure was examined through chemical etching in a 5% solution of nitric acid. Images of the specimen surface were taken using an Axiovert 25 CA optical microscope and EPIQUANT microscope (Carl Zeiss). The surface relief was imaged using a LEO EVO 50 scanning electron microscope (Carl Zeiss). For X-ray diffraction analysis, an INCA energy dispersive analyzer (Oxford Instruments) was used.

Tests for static tension were performed on an Instron 5582 electromechanical testing machine while tests for cyclic tension on a Biss UTM 150 servohydraulic machine. For optical estimation of strains in fatigue tests and characterization of deformation reliefs, images of the specimen surface were taken with a Canon EOS 550D camera. For construction of displacement vector fields and their subsequent translation to strain components, we used the TOMSC television-optical measuring complex and special software [7]. For strain estimation, we calculated the normalized shear strain intensity [8].

The specimen microhardness was measured with a PMT-3 device at a load of 50 g; the measurements were taken on the flat surface and over the specimen cross-section before and after ion beam treatment. For this purpose, no less than 20 indentations were statistically processed. The specimen nanohardness was measured using an MTS G200 nanoindenter with a Berkovich pyramid indented to a depth of ~1 μm. The objective of these measurements was to compare the data of micro- and nanoindentation and to estimate the structural changes involved in Zr ion beam irradiation of 12Cr1MoV steel. The load in nanoindentation was 50 mN and the averaging was over ten measurements.

Fatigue tests were performed in two modes of cyclic tension: high-cycle fatigue with a maximum load of 2.5 kN (320 MPa) and minimum load of 0.9 kN (115 MPa) and low-cycle fatigue with a maximum load of 2.7 kN (345 MPa) and minimum load of 0.9 kN (115 MPa). The parameters of alternate cantilever bending were the following: amplitude 6 mm, shoulder 51 mm, frequency 9.5 Hz.

3. EXPERIMENTAL RESULTS

3.1. Modified Microstructure

Figures 2a and 2c show the microstructure of the untreated steel representing a mixture of ferrite-pearlite grains. The macrostructure after ion beam treatment was

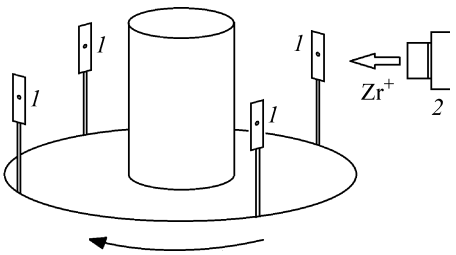

Fig. 1. Schematic of ion beam treatment: *1*—specimens; *2*—ion gun.

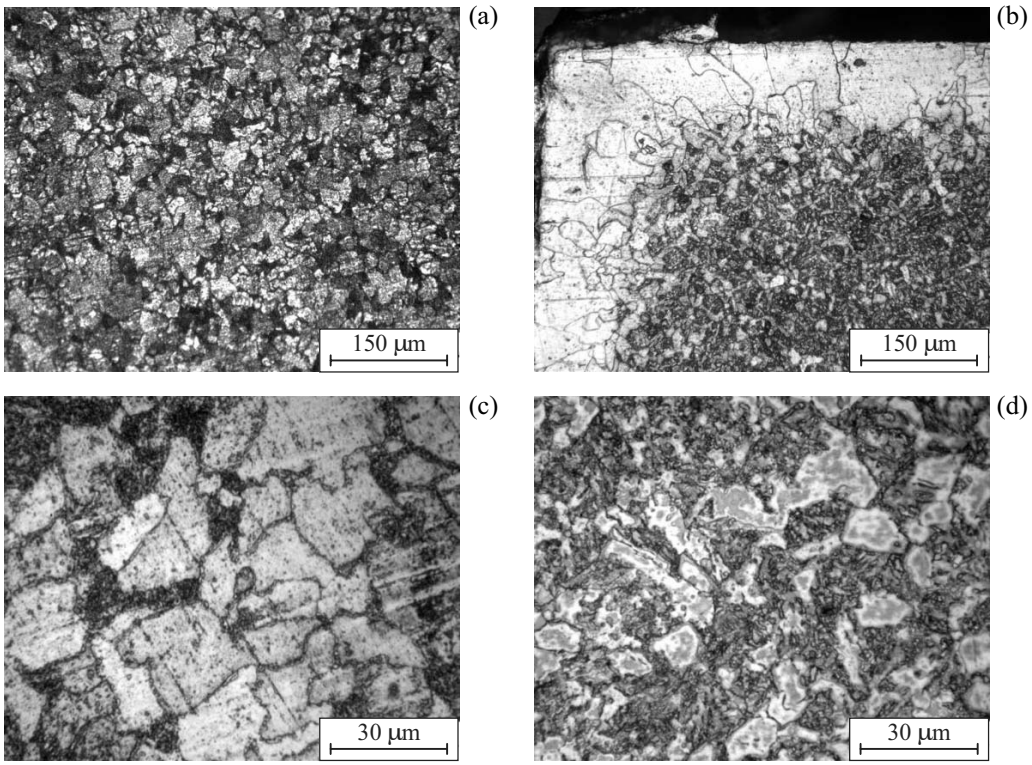

Fig. 2. Optical images of the 12Cr1MoV sections in the as-received state (a, c) and after Zr^+ ion beam treatment (b, d).

analyzed on lateral sections to estimate the modified layer depth (Fig. 2b). As expected, ion beam irradiation modifies not only a thin surface layer due to Zr ion penetration but also deeper matrix (core) layers. The modified layer of thickness 90–130 μm with a clear white hue on etching is characterized by rather coarse grains. However, any clearly defined interface with underlying core layers escapes detection. The cause for the so considerable increase in surface grain size in this type of steel can be heating to high temperatures (to about 900°C). At the same time, the initial grain structure in the core is preserved which can be due to periodic cooling of the specimens in their rotation with respect to the ion beam. Moreover, thermal cycling of the irradiated material results in fragmentation and decreases the grain size from 30–50 μm (Fig. 2c) to $d \le 20$ μm (Fig. 2d). Analysis of the images shows that the observed structure is more typical for troostite-sorbite phases. The internal structure in the core is modified with attendant increase in microhardness compared to the untreated material (Fig. 3).

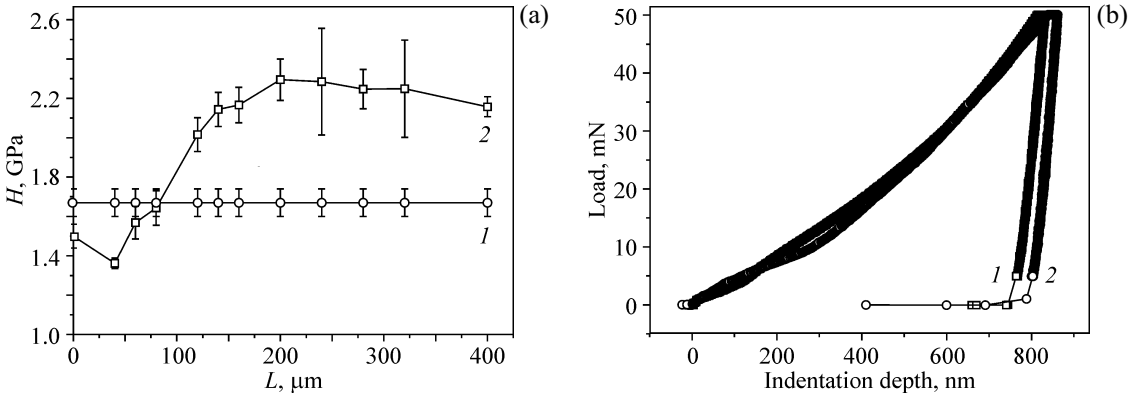

Fig. 3. In-depth variation of the microhardness (a) and nanohardness at a load of 50 mN (b) for 12Cr1MoV steel before (*1*) and after ion beam treatment (*2*).

Table 1. Results of nanoindentation

Specimen type	Hardness, GPa	Elastic modulus, GPa
Untreated	3.5 ± 0.5	226.5 ± 13.5
Treated	2.8 ± 0.6	237.4 ± 26.0
Change after treatment	↓ 20%	↑ 5%

3.1.1. Microhardness and Nanoindentation

The microhardness of the untreated specimens is 1.67± 0.1 GPa. After the ion beam treatment, its value varies greatly with depth from the surface (Fig. 3a). The microhardness on the irradiated surface decreases to 1.5 ± 0.1 GPa. Reasoning from the indentation diagonal, the penetration depth of the Vickers pyramid is 16 μm. The softening is likely due to the temperature which can reach 600–900°C in local surface regions during irradiation. At a depth of 40–50 μm from the surface, the microhardness decreases to 1.45 ± 0.04 GPa, and at a depth of 50–150 μm, it increases to a constant value of about 2.16 ± 0.1 GPa and thus remains higher than the microhardness of the untreated specimens ($H_\mu \sim 1.7$ GPa). These results agree well with the data of optical microscopy (Fig. 2b). Thus, the microhardness of the specimens after ion beam treatment decreases through a depth of about 100–150 μm from the surface, whereas its value at a larger depth increases by ~22%.

The results of nanoindentation at a Berkovich pyramid penetration depth of 900 nm are presented as loading–unloading curves in Fig. 3b and are summarized in Table 1. It is seen that the modified thin surface layer of up to 1 μm thick features a lower nanohardness and slightly increased Young's modulus. The data agree with our previous results [1] and with the data on microindentation (Fig. 3a).

3.1.2. X-ray Diffraction Microanalysis

The content of chemical elements over the cross-section of the untreated and treated specimens is presented in Fig. 4. It is seen in the diagrams that near the surface the content of Cr, Mn, Si, and Fe decreases and the carbon content increases. The chemical compositions of the untreated and treated specimens are rather close at a depth of more than 100 μm from the surface. In the core region at a depth of ~400 μm, the content of the elements differs within the measurement error.

3.2. Static Tension

For more detailed study and quantitative estimation of deformation processes under static tension, we tested the untreated and treated specimens with a double gage section. Diagrams of tensile loading and shear strain intensity are shown in Fig. 5; summarized data on main mechanical properties are presented in Table 2. It is seen that that the ultimate strength after ion beam treatment increases by 10% and the elongation decreases by 19%. These data agree well with our previous tests of dumbbell-shaped specimens [1]. Noteworthy in analyzing the data is that the difference in mechanical properties of two specimen types is likely due to structural modification over the entire specimen cross-section rather than to an "implanted" surface layer of no more than 2 μm.

Another important feature is that the ultimate strength of both specimen types is attained when the strain degree measures less than a half of the total elongation before fracture. This fact was already discussed as applied to 25Cr1Mo1V steel [9]. On the one hand, the specimens are characterized by noticeable strain hardening at the parabolic stage of deformation; on the other hand, when they reach their ultimate strength, they are

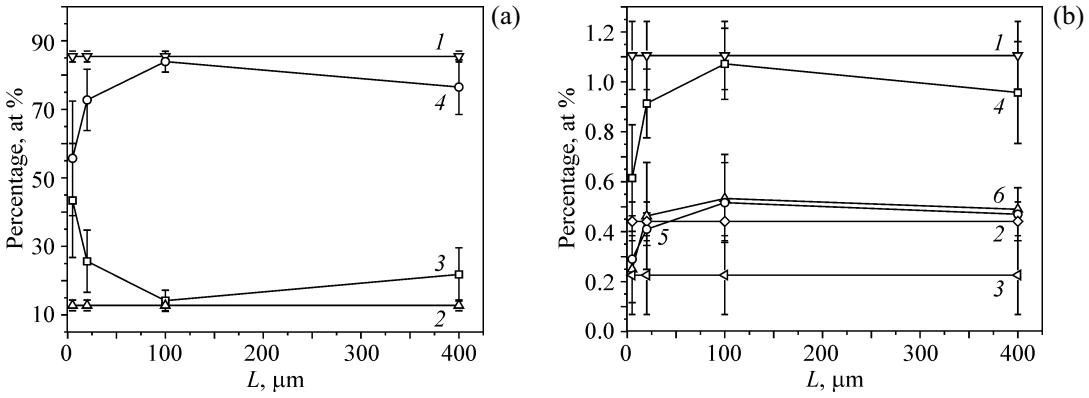

Fig. 4. Atomic percentage of chemical elements in depth from the specimen surface: a—Fe (*1*) and C (*2*) before irradiation, and C (*3*) and Fe (*4*) after irradiation; b—Cr (*1*), Mn (*2*), and Si (*3*) before irradiation, and Cr (*4*), Mn (*5*), and Si (*6*) after irradiation.

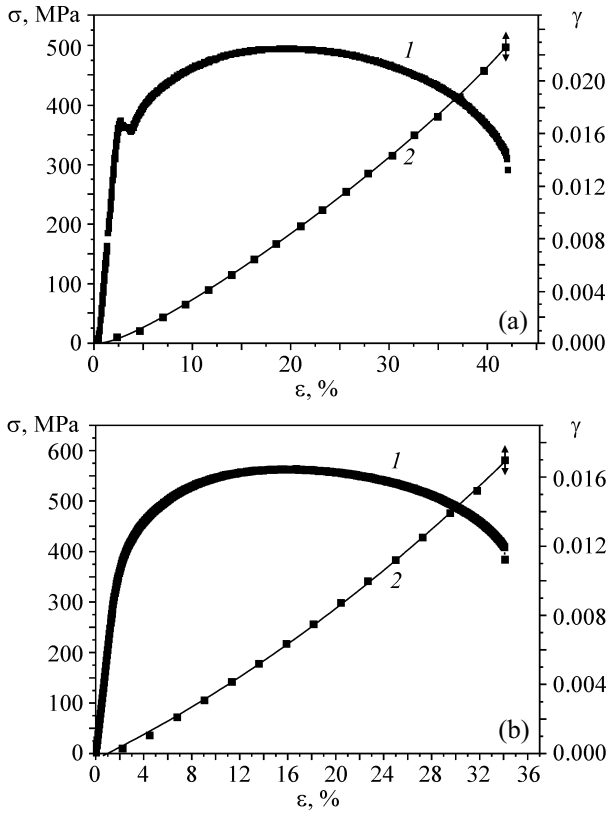

Fig. 5. Tension diagram (*1*) and shear strain intensity (*2*) for the specimens before (a) and after ion beam treatment (b).

rather long deformed without necking. This deformation behavior remains the same after ion beam treatment of 12Cr1MoV steel.

During the tests, images of the specimen surface were taken at an interval of 5 s. Then, the optical images were computer processed to calculate the vector-field average (normalized value) of the shear strain intensity with increasing elongation (Fig. 5). The trends of the curves suggest that the shear strain intensity increases almost linearly with strain. For the untreated specimen, the maximum shear strain intensity (before fracture $\gamma \approx 23\times10^{-3}$) is 26% higher than that for the treated specimen ($\gamma \approx 17\times10^{-3}$). For quantitative and qualitative comparison of the shear strain intensity in both specimens, the distribution fields of this parameter were analyzed (Fig. 6). For correct calculation of the displacement vector fields and strain fields, a mask was superimposed on the images of the specimen after irradiation; the procedure is described in detail elsewhere [2]. The specificity of mask superimposition on the irradiated specimen image gives the impression that a neck is formed even early in the loading; however, this effect should be considered as an artifact.

Table 2. Results of tensile tests for the specimens with a double gage section

Specimen type	Elongation, %	Ultimate strength, MPa
Untreated	42.0 ± 0.1	500 ± 27
Treated	34.0 ± 1.4	555 ± 44

It is seen that early in the loading (Fig. 6a), the untreated specimen reveals a Chernov–Lüders band oriented at an angle to the load axis. In the treated specimen, this effect is not observed (Fig. 6e). Further in the loading, the strain distribution over the gage section of the untreated specimen becomes more uniform (Fig. 6b), and the maximum shear strain intensity is found mostly near the center of the observation region: $\gamma_{max} \approx 285\times10^{-3}$ at $\varepsilon = 16\%$. For the treated specimen at the same strain degree, the strain localization in the centre of the observation region is more pronounced (Fig. 6f); the maximum shear strain intensity reaches $\gamma_{max} \approx 366\times10^{-3}$.

The further loading involves a gradual decrease in the size of the strain localization region at the center of the specimen. In the untreated specimen, the maximum shear strain intensity reaches $\gamma \approx 508\times10^{-3}$ at an elongation of $\varepsilon = 23\%$; in the treated specimen, the maximum shear strain intensity in the region under study is noticeably higher: $\gamma \approx 732\times10^{-3}$. Before fracture, the total strain is localized in a thin macroband located roughly at the centre of the gage section and oriented normal to the direction of applied external load. The shear strain intensity increases almost an order of magnitude and is $\gamma \approx 3640\times10^{-3}$, whereas the shear strain intensity in the treated specimen before fracture is lower and is $\gamma \approx 2720\times10^{-3}$. It should be noted that the observed variation in the shear strain intensity in the region under study agrees well with the data on deformation reliefs, which is an additional support for correctness of the optical method of strain estimation.

The same character of gradual plasticity exhaustion under static tension was demonstrated elsewhere [10, 11]. The behavior of a loaded solid was compared with elastic vibration of a string and the formation of a neck was considered as a process of gradual reduction of the specimen region in which such "elastoplastic waves of local curvature" can propagate [11].

In the treated specimen, no Chernov–Lüders band is formed (Fig. 6e). This agrees well with the absence of a sharp yield point characteristic for low-carbon steels on the loading diagram. Next, the treated specimen is deformed in the same way as the untreated one, except that its maximum shear strain intensity γ in the observation region is higher. Before fracture, the treated specimen

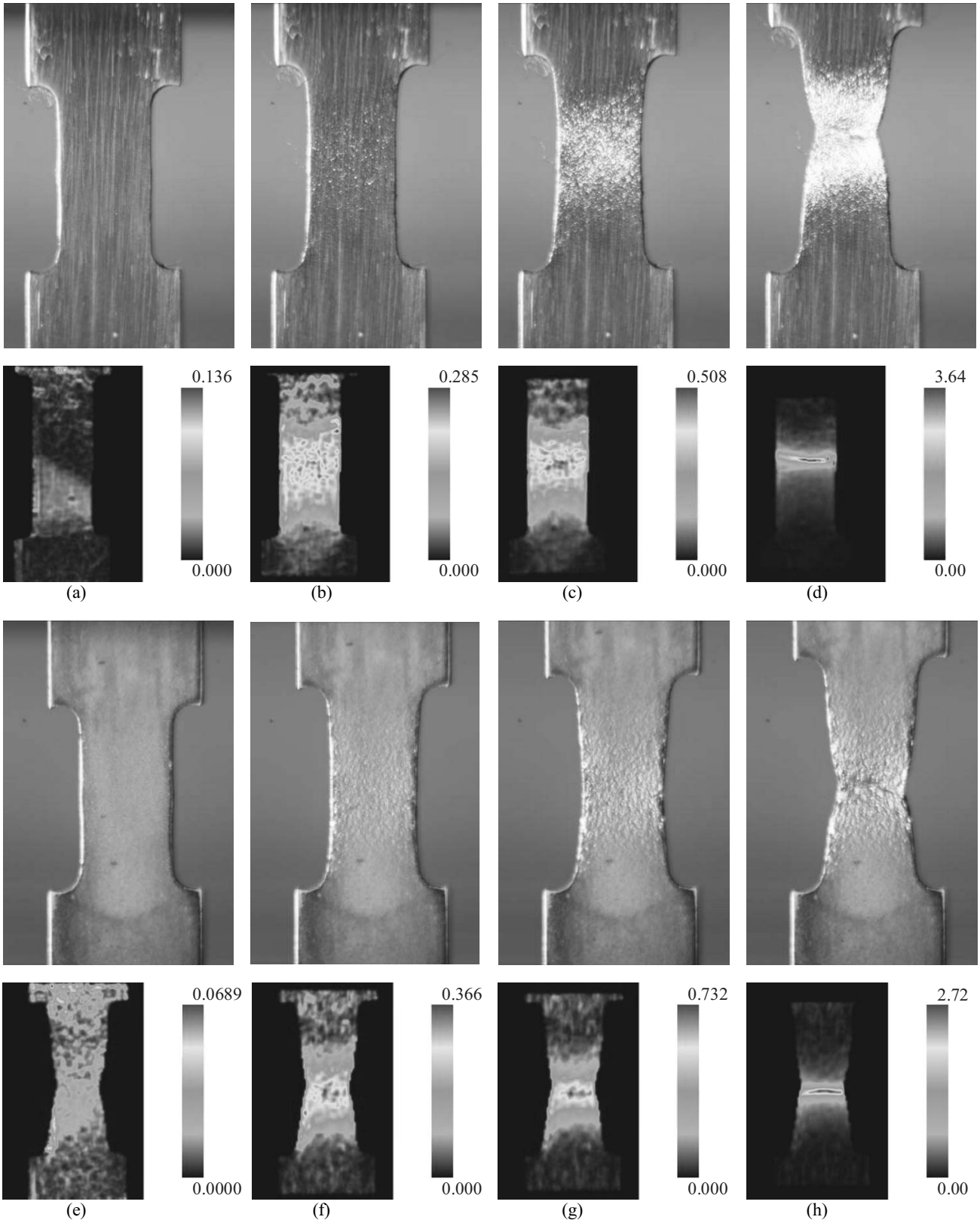

Fig. 6. Images, displacement vector fields, and shear strain intensity distribution for the specimens with a double gage section under tension: untreated material (a–d), treated material (e–h); ε = 3 (a, e), 16 (b, f), 23 (c, g), 34 (h), and 42% (d), fracture (d, h).

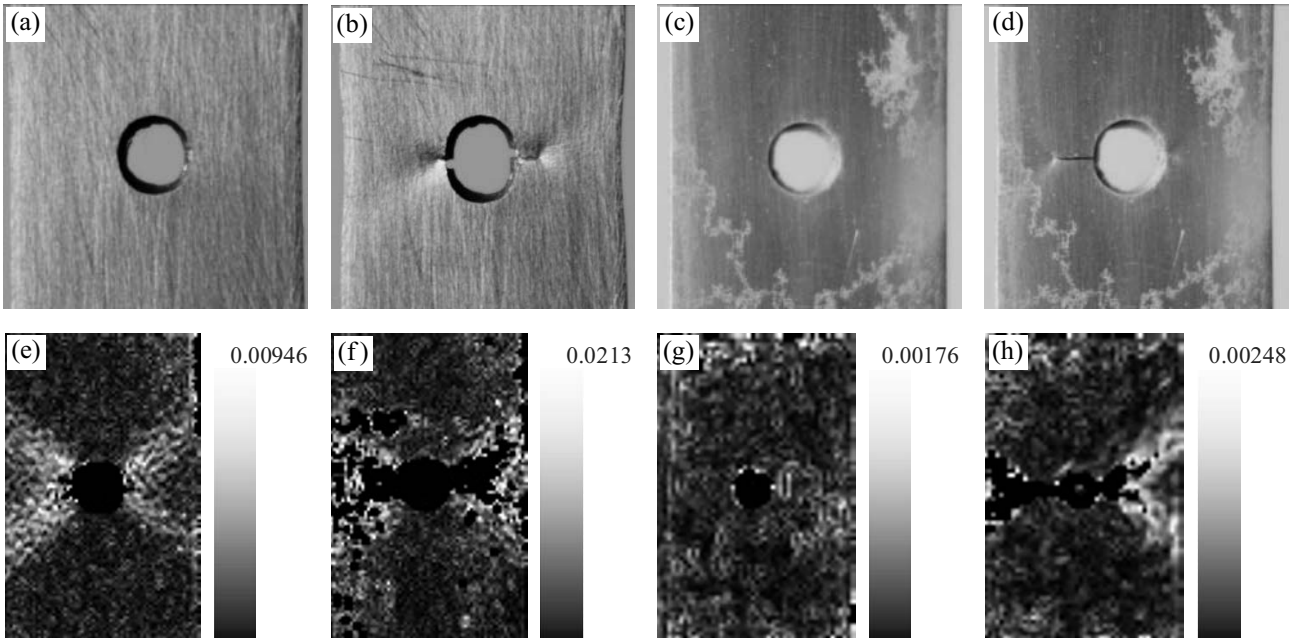

Fig. 7. Optical images (a–d) and shear strain intensity distributions (e–h) at a minimum load of 0.9 kN: untreated material (a, b, e, f), treated material (c, d, g, h); 1000 (a, e, c, g), 44000 (b, f), and 150000 (d, h).

also reveals a strain localization macroband along which a main crack propagates (Fig. 6h).

3.3. Cyclic Tension

3.3.1. Low-Cycle Fatigue and Shear Strain Intensity

Our previous tests for cyclic tension and bending show that ion beam treatment can provide a considerable increase in fatigue life [1]. In the paper presented, our aim was to clarify the features of meso- and macroscale deformation by the digital image correlation method. Figure 7 shows optical images and shear strain intensity distributions for the treated and untreated specimens in low-cycle fatigue. It is seen that cross-shaped macrobands of strain localization not found on the optical images develop in the untreated specimens in the direction of maximum tangential stresses even after the first thousand of cycles (Fig. 7e). This is due to a rather high level of applied external load (345 MPa) which approximates the yield strength of the ductile steel. At this loading stage, the average shear strain intensity in the region under study is $\gamma \approx 14\times10^{-3}$ (Fig. 8, curve *1*). At the next loading stage, two main fatigue cracks in the region of minimum cross-section develop in opposite directions perpendicular to the load axis (Fig. 7b). This corresponds to the increase in average shear strain intensity in

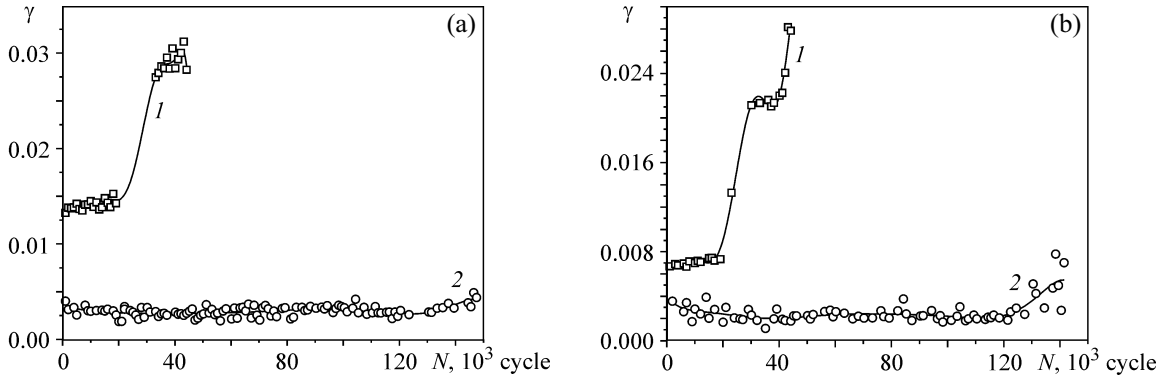

Fig. 8. Average shear strain intensity versus the number of cycles at two loads: a—0.9 kN (115 MPa), b—2.7 kN (345 MPa); *1*—untreated material, *2*—treated material.

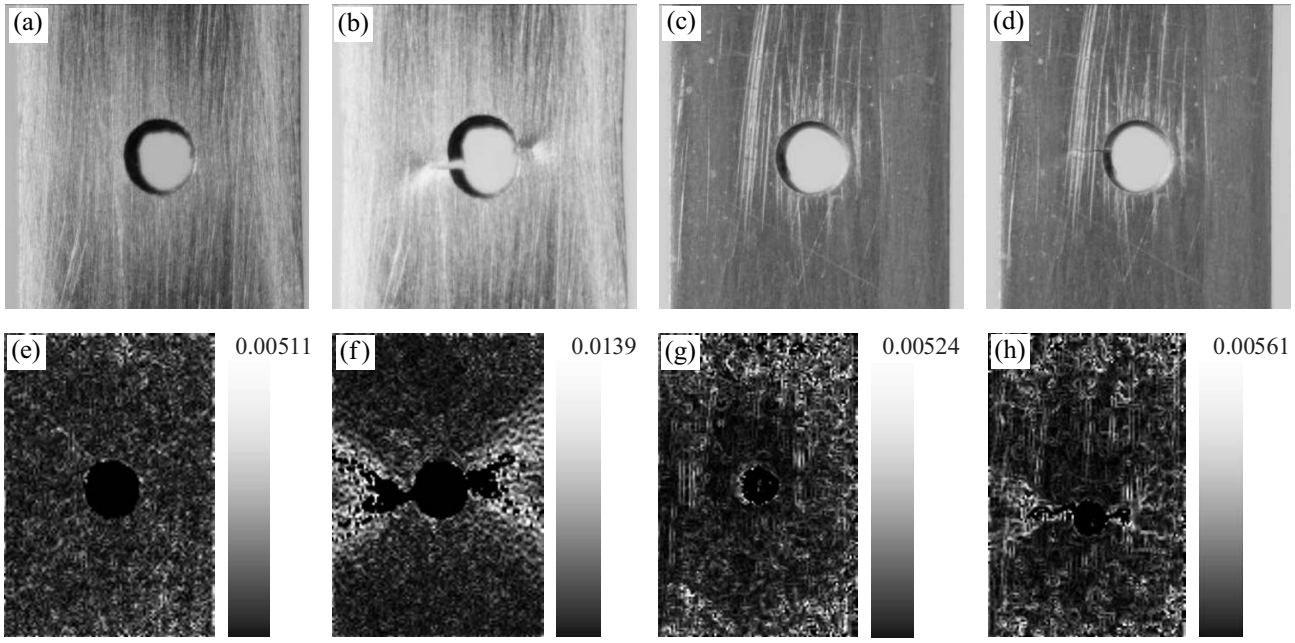

Fig. 9. Optical images (a–d) and shear strain intensity distribution (e–h) at a load of 2.5 kN: a, b, e, f—untreated material; c, d, g, h—treated material; 61000 (a, e), 122000 (b, f), 193000 (c, g), and 247000 cycles (d, h).

the observation region to $\gamma \approx 30\times10^{-3}$, which is bound to result from severe plastic deformation involved in opening of both cracks (Fig. 8, curve *1*).

In the treated specimen, due to structural modification over its cross-section, no macrobands of strain localization are observed under cyclic loading (Figs. 7c and 7g). This is supported by the average shear strain intensity which is more than two times lower in the observation region for the treated specimen compared to the untreated one (Fig. 8, curve *2*). In the specimens subjected to ion beam treatment, changes in the strain intensity distributions are observed only before fracture (N = 150000 cycles, Figs. 7d and 7h).

The dependences of the average shear strain intensity on the number of cycles at different levels of applied load (Fig. 8a) reveal two characteristic stages. The diagram for the untreated specimen has two characteristic portions: a portion which precedes propagation of a crack and a portion which corresponds to propagation of main fatigue cracks when the average shear strain intensity increases to over $\gamma \geq 27\times10^{-3}$. For the treated specimen, individual stages escape detection almost to the point of fracture and its shear strain intensity starts gradually increasing only at $N \geq 120\times10^{3}$ cycles, which also corresponds to nucleation and propagation of fatigue cracks. The disclosed mechanisms allow us to adequately explain the cause for fatigue life enhancement in the specimens subjected to ion beam treatment. Figure 8b shows the same dependences but calculated by the DIC method at a maximum load of 2.5 kN. By and large, the stage character of the curves is preserved, and the absolute value of the analyzed parameter decreases about two times.

3.3.2. High-Cycle Fatigue

Figures 9a and 9c present optical images of the surface for the treated and untreated specimens under cyclic tension shortly before fracture. Similarly to the low-cycle fatigue tests, the untreated specimen reveals a crack nucleating in the region of minimum cross-section with the formation of two conjugate strain localization bands (Fig. 9b). The fracture region is characterized by noticeable contraction of the specimen and formation of a clearly defined strain-induced relief. The surface of the treated specimens is smoother, the deformation relief is not formed, and the contraction is much less pronounced (Fig. 9d).

Figures 9e–9h show shear strain intensity distributions for the treated and untreated specimens tested in the mode of high-cycle fatigue; the images were taken at a load of 2.5 kN. It is seen that near the hole of the untreated specimens after N = 60000 (the total number of cycles before fracture is N_p = 122000), strain localization macrobands develop in the direction of maximum tangential stresses. Under further cyclic loading, the strain localization macrobands in the form of a cross become more pronounced, particular after the onset of fatigue crack growth (Fig. 9e, N = 122000 cycles). In the treated specimens, noticeable changes in the strain

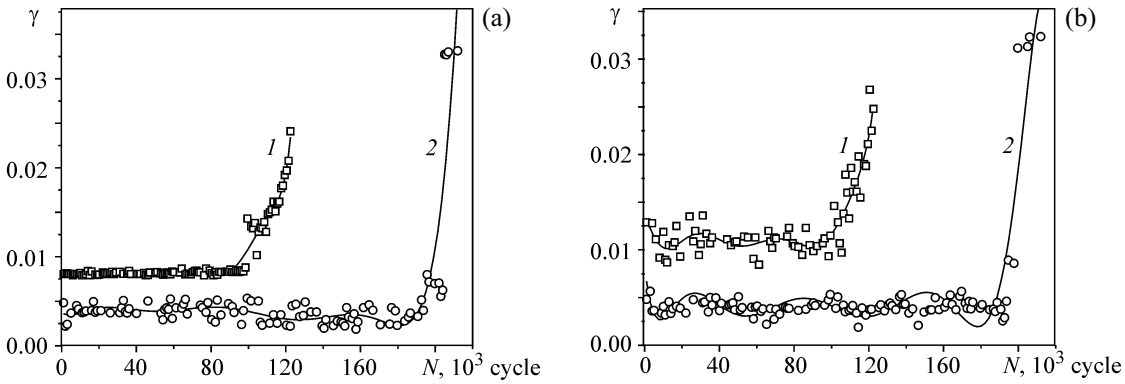

Fig. 10. Average shear strain intensity vs the number of cycles: a—0.9 kN (115 MPa), b—2.5 kN (320 MPa); *1*—untreated material, *2*—treated material.

intensity distribution are observed only before fracture (Fig. 9h, 247000 cycles).

The foregoing results become more obvious if we analyze the average shear strain intensity against the number of loading cycles (Fig. 10). Figure 10a shows diagrams obtained by optical data processing at the minimum load. It is seen that like in the low-cycle fatigue tests, the shear strain intensities for both specimen types differ about two times ($\gamma \approx 0.4\times10^{-3}$ and 0.7×10^{-3} for the untreated and treated specimens, respectively). However, the stage patterns in the modes of low- and high-cycle fatigue differ markedly due to the difference in the time of fatigue crack nucleation. The data on high-cycle fatigue in normalized coordinates show that the fatigue crack in this mode nucleates later. For the same reason, the second stage is much shorter and the increase in shear strain intensity at the second stage is several times greater compared to the mode of low-cycle fatigue. For the treated specimen, this parameter changes in a similar way. The above data are supported by the diagram of the shear strain intensity calculated through image processing at a maximum load of 2.5 kN (Fig. 10b).

Thus, the degree of fatigue life enhancement in the mode of low-cycle fatigue is noticeably higher compared to the mode of high-cycle fatigue. This is because the contribution of the modified surface layer (of up to several tens of micrometers) to the fatigue crack resistance decreases, and once a fatigue crack arises, the fracture patterns in both modes are similar.

3.4. Alternate Cyclic Bending

Figure 11 shows dependences of the crack length on the number of cycles; the diagrams were constructed from the images taken in mechanical tests. The same figure presents images of the specimens in the stress concentrator region at the initial stage (soon after crack nucleation) and shortly before fracture. It is seen that both specimen types reveal crack nucleation at about the same number of cycles. However, the growth rate of the main fatigue crack in the untreated specimen is much higher. A more detailed description of these results can be found in our previous paper [1].

Figure 12 shows displacement vector fields for the untreated and treated specimens. The vector fields for the untreated specimens (Figs. 12a and 12c) represent displacements typical for brittle-ductile growth of a fatigue crack [12] when opening of its tip is preceded by translational-rotational vortex motion of material. In the region of crack growth, a clearly defined deformation relief in the form of slip traces and folds at grain boundaries arises (Fig. 12a). In our opinion, the fatigue crack propagates through coalescence of microcracks at the boundaries of structural elements. At the next stage of fatigue fracture [12], the mechanism of crack growth can be characterized as opening mode cracking (Figs. 12e and 12g). Despite the branching of its tip, the displacements at both crack edges unambiguously suggest that the crack opening occurs by the above mechanism. The substantial stress concentration at the crack tip governs the formation of a pair of strain localization bands in the direction of maximum tangential stresses (Fig. 12g).

The treated specimens reveal another character of deformation (Figs. 12c, 12d, 12g, 12h). On their surface, quite many mesoscale strain-induced defects are observed and mostly as folds of extruded material (Fig. 12b), which owes to the pattern of alternate cantilever bending. Several surface microcracks with noticeable branching propagate at a time from the hole as a stress concentrator. This fact becomes clear from analysis of the displacement vector field (Fig. 12d). It is seen that due to dispersion of the powerful stress macroconcentrator and

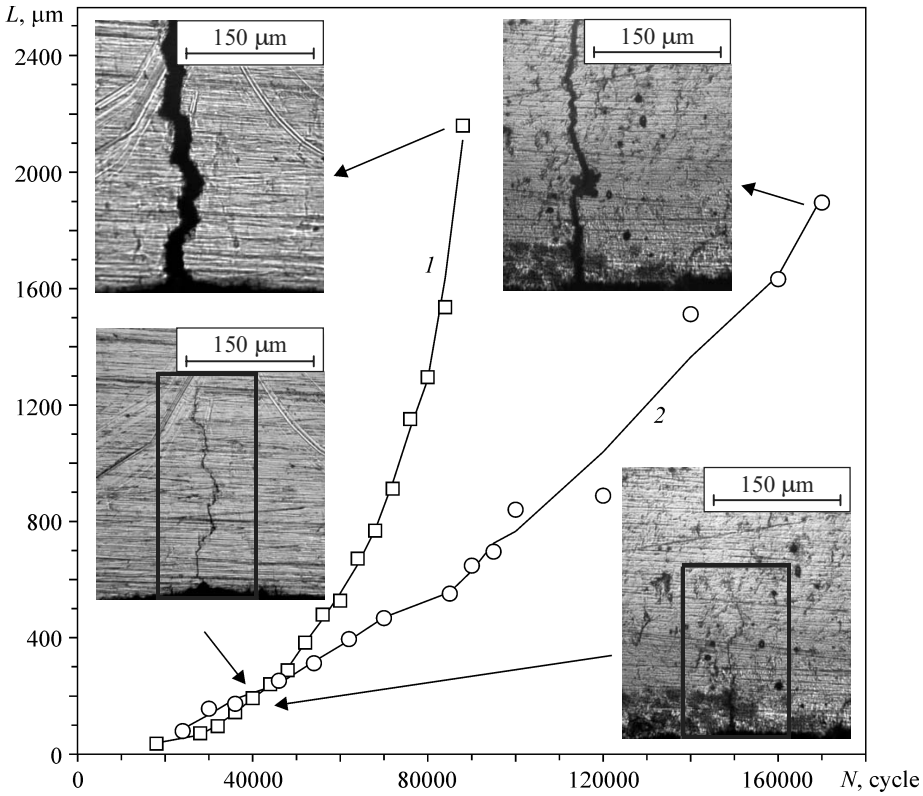

Fig. 11. Crack length versus the number of cycles: *1*—untreated material, *2*—treated material.

formation of a large number of mesoscale defects, the deformation is less localized and this impedes the nucleation and subsequent propagation of a main fatigue crack (Fig. 11, curve *2*).

As the number of loading cycles is increased to $N = 15\times10^3$, the main crack grows with attendant substantial fragmentation of the surrounding material: the displacement vector field reveals clearly defined regions with identical displacement directions (Fig. 12h). The crack propagation mechanism, in this case, can hardly be treated as opening mode cracking. Thus, the structural modification of the surface to a depth of tens of micrometers changes the character of fatigue crack nucleation and propagation and increases the fatigue life of the material about two times. It should be noted that although the change from cyclic tension to bending changes the influence of the modified surface layer on the mechanisms of fatigue crack growth, the modification does provide a considerable increase in the fatigue life of the material.

5. DISCUSSION OF THE RESULTS

The results obtained in the study can have a dual interpretation. On the one hand, the modification increased the fatigue life more than two times, and on the other hand, the hardness of the near-surface layer was noticeably decreased thus making the effect of Zr ion doping less positive. In terms of fatigue crack resistance, it is preferable to retard the deformation processes in the surface layer, which does take place according the data on deformation reliefs. At the same time, it is desirable not to impair the hardness of the underlying layers. A similar effect is attained by surface nanostructuring through ultrasonic treatment [6] which increases the microhardness at a depth of several hundred micrometers. In this case, the increase in fatigue life is bound to be greater. This issue is the subject of our future studies.

Particularly noteworthy is the result presented in Fig. 11. It is seen that the specimen after ion beam treatment undergoes fatigue fracture with a lesser degree of crack opening compared to the untreated one. This correlates well with lower crack velocities. The curvature at the crack tip is proportional to the number of curvature vacancies [13] which nucleate in the region and provide the possibility for further crack growth. The foregoing fact gives an insight into the cause for the lower fatigue crack velocity in the treated specimen and hence its higher fatigue life.

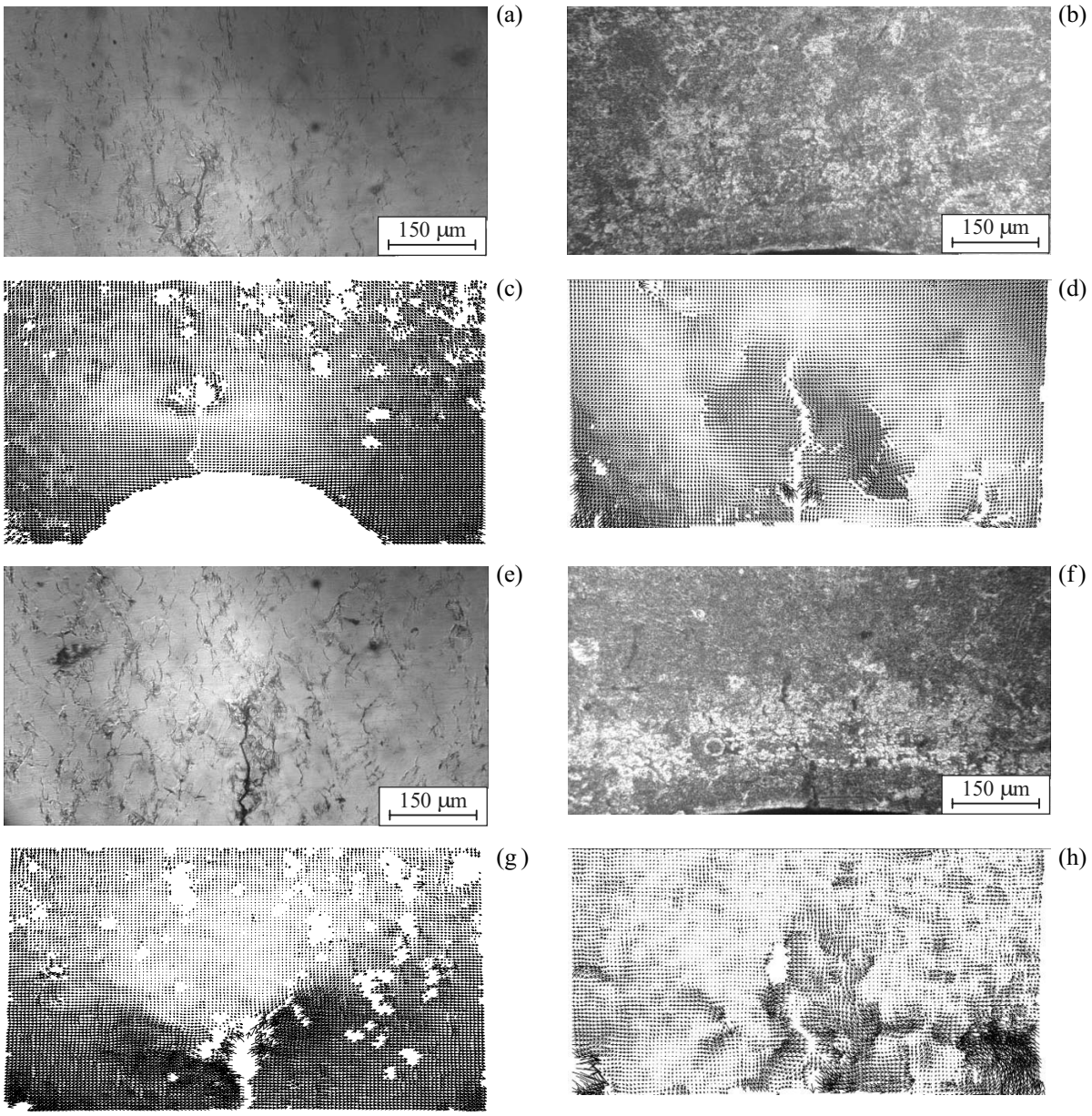

Fig. 12. Optical images and corresponding displacement vector fields under cyclic bending: untreated material (a, c, e, g), treated material (b, d, f, h): a, c—$(3 \div 4)\times10^3$, b, d—$(1 \div 45)\times10^3$, e, g—$(19 \div 20)\times10^3$, f, h—$(3 \div 25)\times10^3$ cycles. The stress concentrator is at the bottom.

Compared to the untreated specimens, the specimens subjected to ion beam irradiation reveal complex structural transformation over their cross-section. In a surface layer of several micrometers, softening is observed (nanoindentation); in a layer of up to 120 μm, heat-induced softening takes place (microindentation); and in the core, the microhardness increases due to the processes induced by local ion beam heating. This, as a whole, increases the yield stress of the material under tension and its fatigue life. However, this mode of treatment cannot be considered optimum, and our further efforts will be put into searching for such conditions that provide minimum thermal action on the matrix during Zr ion beam irradiation.

6. CONCLUSION

Thus, it is shown that the 12Cr1MoV specimens of thickness 1 mm subjected to irradiation with a Zr ion beam undergo structural modification over the entire cross-section. The microhardness in their surface layer of up to 100 μm decreases, while its value in the core in-

creases compared to the untreated specimens. The modification increases the iron percentage and decreases the carbon percentage in the surface layer.

The quantitative and qualitative estimates made for the shear strain intensity by the digital image correlation method demonstrate that the treated specimens, due to their structural changes over the entire cross-section, experience earlier strain localization at the center of the gage section.

The data of fatigue tests show that under cyclic tension, the modified structure of the irradiated specimens retards the localization of plastic strains before nucleation and during propagation of a main fatigue crack, and this decreases the average shear strain intensity. As a result, the fatigue life of modified 12Cr1MoV steel can increase two times.

The treatment considered in the paper cannot be characterized as surface modification because the structure is modified through large depths due to high local temperatures. The observed changes in mechanical properties under static and cyclic loads should be interpreted in the context of the loaded specimens as a multiscale system: (1) a Zr-doped surface layer of several micrometers, (2) a thermally softened layer of up to 100–120 μm, and (3) a core hardened due to short-time cyclic thermal action. The most efficient behavior of the multiscale system is observed under cyclic loading.

The work was performed under the fundamental research program of the State Academies of Sciences for 2013–2020 and was partially supported by RFBR project No. 15-08-05818 and by grant of the President of the Russian Federation for support of leading scientific schools NSh-2817.2014.1. The equipment for scanning electron microscopy and X-ray diffraction analysis was provided by the Nanotekh Shared Use Center of ISPMS SB RAS.

REFERENCES

1. Panin, S.V., Vlasov, I.V., Sergeev, V.P., Sungatulin, A.R., Kalashnikov, M.P., Poltaranin, M.A., and Ovechkin, B.B., Increasing the Fatigue Life of 12Cr1MoV Steel by Surface Nanostructuring with a Zr^+ Ion Beam. Structure, Properties, and Fracture Pattern, *Phys. Mesomech.*, 2013, vol. 16, no. 2, pp. 170–182.
2. Sutton, M., Orteu, J.J., and Schreier, H., *Image Correlation for Shape, Motion, and Deformation Measurements*, New York: Springer, 2009.
3. Dombrovskii, F.S. and Leschinskii, L.K., *Operability of Clad Continuous Casting Rolls*, Kiev: E.O. Paton Electric Welding Inst., NANU, 1995.
4. Yasniy, P., Maruschak, P., Bishchak, R., Hlado, V., and Pylypenko, A., Damage and Fracture of Heat Resistance Steel under Cyclic Thermal Loading, *Theor. Appl. Fract. Mech*., 2009, vol. 52, pp. 22–25.
5. Zubchenko, A.S., Koloskov, M.M., Kashirskii, Yu.V., et al., *Grades of Steels and Alloys*, Zubchenko, A.S., Ed., Moscow: Mashinostroenie, 2003.
6. Panin, V.E., Sergeev, B.P., and Panin, A.V., *Surface Nanostructuring of Structural Materials and Deposition of Nanostructured Coatings*, Tomsk: Tomsk Polytechnic Univ., 2008.
7. Lyubutin, P.S. and Panin, S.V., Mesoscale Measurement of Strains by Analyzing Optical Image of the Surface of Loaded Solids, *J. Appl. Mech. Tech. Phys*., 2006, vol. 47, no. 6, pp. 905–910.
8. Filin, A.P., *Applied Mechanics of Deformed Solids*, Moscow: Nauka, 1975, vol. 1.
9. Maruschak, P.O., Panin, S.V., Student, A.Z., and Ovechkin, B.B., *Strain and Fractures Scales in Heat-Resistant Steels*, Pichugin, V.F., Ed., Tomsk: Tomsk Polytechnic Univ., 2013.
10. Panin, V.E., Grinyaev, Yu.V., and Egorushkin, V.E., Foundations of Physical Mesomechanics of Structurally Inhomogeneous Media, *Mech. Solids*, 2010, no. 4, pp. 501–518.
11. Panin, V.E., Elsukova, T.F., Egorushkin, V.E., Vaulina, O.Yu., and Pochivalov, Yu.I., Deformation Mechanisms and Mass Transfer in Highly Nonequilibrium Polycrystals in Alternate Bending, *Deform. Razr. Mater.*, 2009, no. 6, pp. 2–12.
12. Panin, V.E., Pleshanov, V.S., and Kibitkin, V.V., Evolution of Strain Domains and Kinetics of Mesoscale Fatigue Fracture in Duralumin Polycrystals, *Pis'ma Zh. Tekh. Fiz*., 1997, vol. 23, no. 24, pp. 51–57.
13. Panin, V.E., Elsukova, T.F., Vaulina, O.Yu., and Pochivalov, Yu.I., Nonlinear Wave Effects of Curvature Solitons in Surface Layers of High-Purity Aluminum Polycrystals under Severe Plastic Deformation. II. The Role of Boundary Conditions, Interfaces, and Nonequilibrium of a Deformed State, *Phys. Mesomech*., 2008, vol. 11, no. 5–6, pp. 299–307.